REPORT DOCUMENTATION PAGE

Form Approved
OMB No. 0704-0188

1. REPORT DATE *(DD-MM-YYYY)*	2. REPORT TYPE	3. DATES COVERED *(From - To)*
3/30/2011	Final Report	4/1/2007 – 2/28/2011

4. TITLE AND SUBTITLE
A Next-Generation Model of the Corona and Solar Wind

5a. CONTRACT NUMBER
FA9550-07-C-0044

5b. GRANT NUMBER

5c. PROGRAM ELEMENT NUMBER

6. AUTHOR(S)
Linker, Jon, A.

5d. PROJECT NUMBER

5e. TASK NUMBER

5f. WORK UNIT NUMBER

7. PERFORMING ORGANIZATION NAME(S) AND ADDRESS(ES)

Science Applications International Corporation
10260 Campus Point Drive
San Diego, CA 92121

Predictive Science Inc.
9990 Mesa Rim Road, Suite 170
San Diego, CA 92121

8. PERFORMING ORGANIZATION REPORT NUMBER

9. SPONSORING / MONITORING AGENCY NAME(S) AND ADDRESS(ES)
Air Force Office of Scientific Research
875 N Randolph St
Arlington, VA 22203

10. SPONSOR/MONITOR'S ACRONYM(S)
AFOSR

11. SPONSOR/MONITOR'S REPORT NUMBER(S)
AFRL-OSR-VA-TR-2012-0199

12. DISTRIBUTION / AVAILABILITY STATEMENT
UU Unclassified/Unlimited

13. SUPPLEMENTARY NOTES

14. ABSTRACT

A central goal of solar and space physics is to understand the influence of the sun and its activity on the heliosphere, particularly the space environment near the Earth. A quantitative description of the ambient solar corona and solar wind is key to understanding this influence. This report describes important features of CORHEL (for CORona-Heliosphere), a suite of models and tools for modeling the solar corona and inner heliosphere. Support from this project has facilitated further development and key improvements to CORHEL, including the extension to thermodynamic MHD solutions, incorporation of the WSA model for quick look solutions, and the use of multiple solar observatories for magnetic map input.

15. SUBJECT TERMS
Space Weather, Solar Corona, Solar Wind, magnetic fields

16. SECURITY CLASSIFICATION OF: U (Unclassified)			17. LIMITATION OF ABSTRACT	18. NUMBER OF PAGES	19a. NAME OF RESPONSIBLE PERSON
a. REPORT U (Unclassified)	b. ABSTRACT U (Unclassified)	c. THIS PAGE U (Unclassified)	UU (Unclassified/Unlimited)	19	Jon Linker
					19b. TELEPHONE NUMBER *(include area code)* 858-450-6489

A Next-Generation Model of the Corona and Solar Wind: Final Report

AFOSR Contract FA9550-07-C-0044

4/1/2007 - 2/28/2011

AFOSR Program Manager: Dr. Cassandra Fesen

Submitted by

Michael Brown-Hayes, Contract Manager
Science Applications International Corporation
10260 Campus Point Drive
San Diego, CA 92121
(SAIC project serial 5510)

Subcontracted to:

Jon Linker, Principal Investigator
Predictive Science Inc.
9990 Mesa Rim Road, Suite 170
San Diego, CA 92121

March 31, 2011

A Next-Generation Model of the Corona and Solar Wind: Final Report

A Next-Generation Model of the Corona and Solar Wind: Final Report

1 Introduction

A central goal of solar and space physics is to understand the impacts of the Sun and its activity on the heliosphere, particularly the space environment near the Earth. While coronal mass ejections (CMEs) are the most spectacular example of this influence, the structure and dynamics of the ambient solar corona and solar wind is also important. Coronal structure leads to the partitioning of the solar wind into fast and slow streams, which are the source of recurrent geomagnetic activity. The geo-effectiveness of CMEs is in part determined by their interaction with the ambient wind. The connection of the ambient interplanetary magnetic field to CME-related shocks and impulsive solar flares determines where solar energetic particles propagate. If we are to make substantial progress in understanding and predicting the Sun's space weather effects, a quantitative description of the the solar corona and solar wind is essential.

The goal of our project, which has been supported by the joint AFOSR/NASA/NSF partnership for Collaborative Space Weather Modeling, is to improve and further develop a time-dependent, three-dimensional MHD model of the solar corona and solar wind, and to deliver versions of the model for community use. Our project focuses on improving the underlying physics, boundary conditions, and usability of the model in several key areas, as described in this report. The general framework for our coronal and heliospheric solutions is described as "CORHEL" for Corona-Heliosphere. The original version of CORHEL, developed for the CISM (Center for Integrated Space Weather Modeling) project, included the MAS (Magneto-hydrodynamic Algorithm outside a Sphere) code for coronal computations and the Enlil code for heliospheric computations. To minimize confusion and support one deliverable product, we have retained the name CORHEL for the products of this project. As a result of our joint support, the capabilities of CORHEL have been greatly improved and extended. CORHEL now delivers solutions to the community via four customers at the present time: the CCMC, CISM, our own modeling web site (www.predsci.com), and AFRL in Albuquerque. An essential aspect of our modeling approach for CORHEL is the use of different approximations for the coronal solution, and to allow these solutions to provide the inner boundary condition for heliospheric solutions. A flow chart of the key components of CORHEL is given in Appendix A.

The great utility of a coronal and heliospheric modeling suite is the ability to assist in interpreting both remote solar and in situ measurements within a global context. To illustrate this, Figure 1 summarizes the state of the solar corona and inner heliosphere for Carrington rotation (CR) 1922, which occurred from April 24, 1997 through May 21, 1997, and provided the background state into which the well-studied May 12, 1997 CME erupted (Webb et al., 2000; Odstrcil et al., 2004, 2005; Linker et al., 2007). The coronal solution on the left was computed using our most sophisticated thermodynamic model (see section 2.1), while the heliospheric solution on the right was generated using a simplified, empirically based polytropic model. In the following sections we briefly describe the capabilities of the different components of CORHEL.

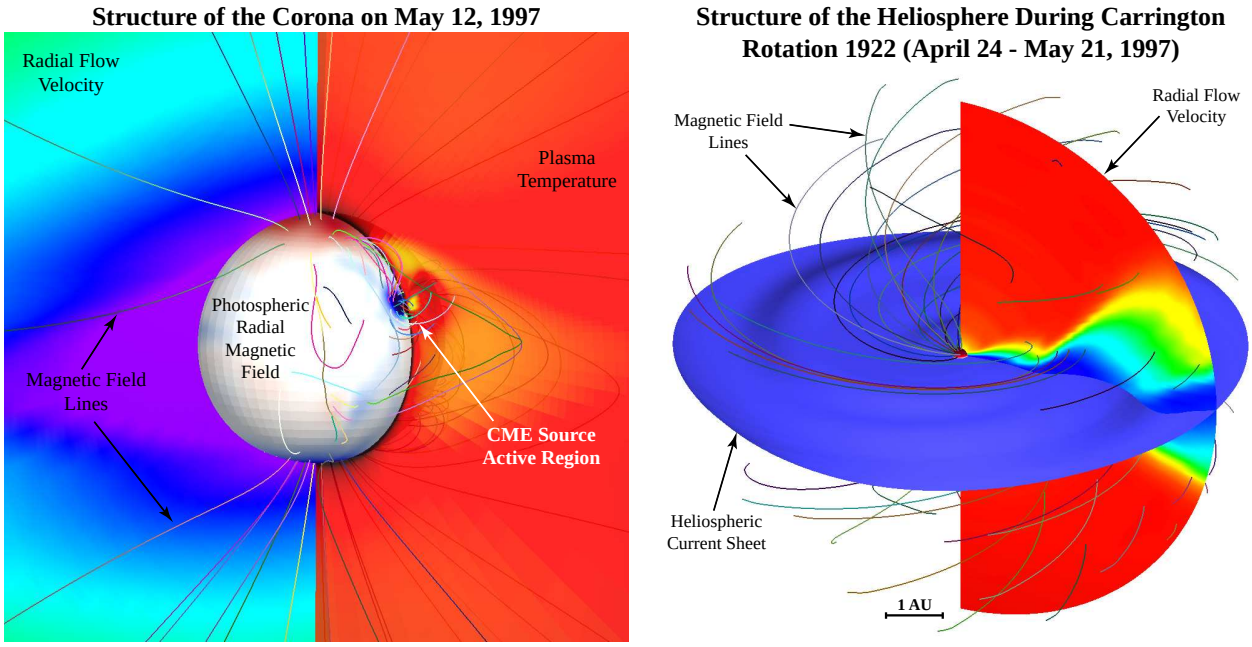

Figure 1: A detailed numerical simulation of a CME can capture the detailed properties of the solar source active region (left), including measured magnetic fields derived from magnetograms, as well as the structure of the background solar wind in the heliosphere (right).

2 The Coronal MHD Model MAS

The PSI coronal code MAS solves the MHD equations on a nonuniform spherical grid that allows us to concentrate grid points in regions of interest. The method of solution, including the boundary conditions, has been described previously (Mikić & Linker, 1994; Linker & Mikić, 1997; Lionello et al., 1999; Mikić et al., 1999; Linker et al., 2001; Lionello et al., 2001). A description of the equations solved in the MHD model is given in Appendix A.1. To compute a coronal solution, the MAS model integrates these time-dependent equations to steady state for a given boundary condition defined by a magnetic map. We commonly speak of two approximations for the model. The polytropic model neglects the complicated physics of the transition region by setting the ratio of specific heats γ to a reduced value. The model retains an energy equation (Eq. (6) in Appendix A.1 with $S = 0$) but we refer to it as polytropic to denote this limitation. We began using this approximation 15 years ago in our first eclipse calculation (Mikić & Linker, 1996) and it remains useful; it is still used in many contemporary MHD models (e.g., Cohen et al., 2008; Hayashi et al., 2008). A more advanced treatment of the energy equation is described below.

2.1 The Thermodynamic MHD Model

A key enhancement in the CORHEL model is the inclusion of important energy-transport processes (radiative losses, anisotropic thermal conduction, and coronal heating) in the transition region and solar corona. We refer to this as the "thermodynamic" MHD model. This more accurate representation of energy flow in the MHD model allows us to compute simulated

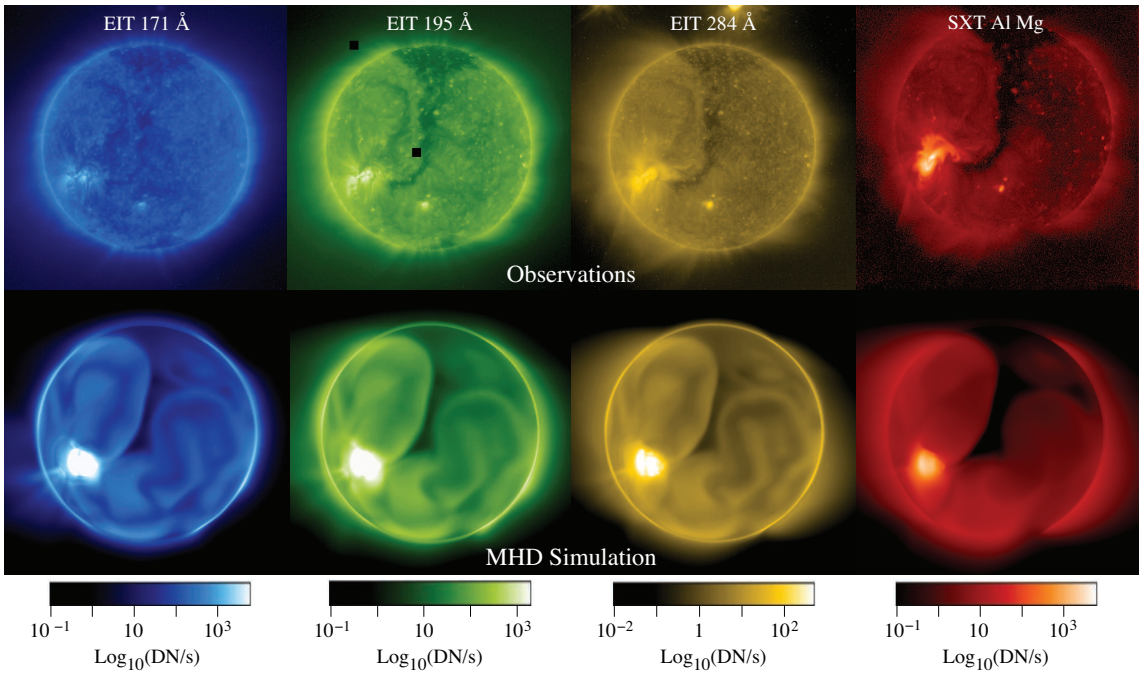

Figure 2: Comparison between the emission observed on August 27, 1996 in SOHO/EIT and Yohkoh/SXT (Top) and a coronal MHD simulation with energy transport terms included in the energy equation (Bottom). The images from the calculation were synthesized by integrating the appropriate emission kernels along the line of sight. Observations and simulations are scaled identically.

EUV and X-ray emission as is observed from instruments such as EIT aboard SOHO, the SECCHI EUV imagers aboard the STEREO spacecraft, the Hinode XRT instrument, and the AIA instrument aboard SDO. Comparison with actual emission provides powerful constraints on the models.

The principal uncertainty in the thermodynamic MHD model arises from the unknown mechanism of coronal heating. Although there has been considerable theoretical activity in understanding coronal heating and acceleration of the solar wind (e.g., Piddington, 1956; Osterbrock, 1961; Parker, 1972, 1994; Roberts, 2000; Velli, 2003; Hollweg, 2003), the details are not understood.

In order to produce models that are consistent with observations, we have developed a parameterized approach for describing the coronal heating (Lionello et al., 2009). Although this limits our ability to address theories of heating in any detail, it does provide a pragmatic compromise of being able to include the chromosphere and transition region within our code and restore the adiabatic index, γ, back to 5/3. Additionally, comparisons between simulated emission (EUV and soft X-ray) and observations provide strong constraints on the free parameters in the heating model (Lionello et al., 2009). We are also developing heating models derived from: (1) an extension of robust scaling laws (Rappazzo et al., 2007) based on Parker's idea of shaking and tangling of magnetic field lines (Parker, 1972) to include shell models of turbulence (Buchlin & Velli, 2007); and (2) Wave/turbulence-driven (WTD) models, which attempt to provide a self-consistent description of both the acceleration and heating of solar

Comparison of Simulated and Observed Emission for Four Different Time Periods

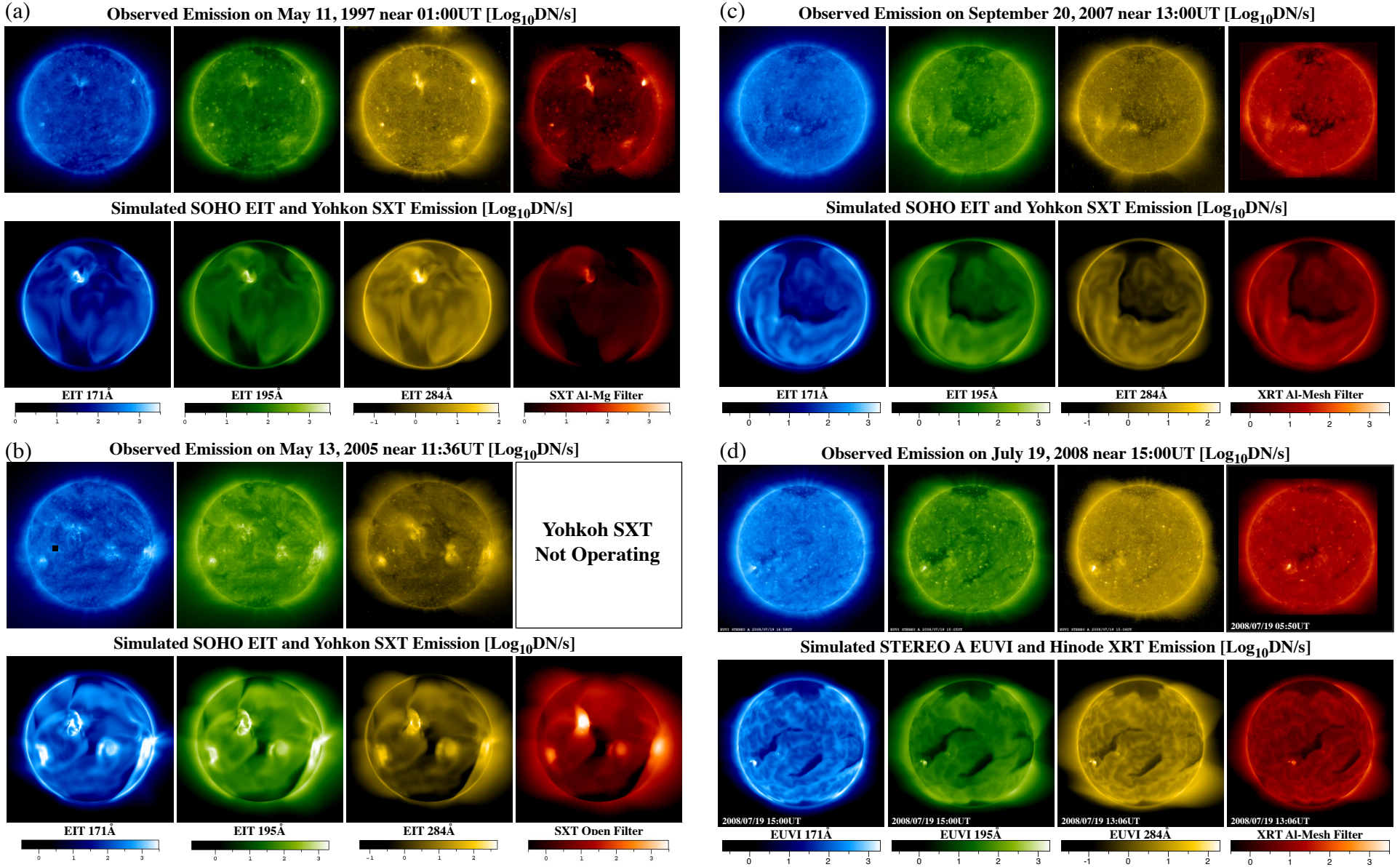

Figure 3. *Comparison of simulated and observed emission for different time periods with the same composite heating model: (a) May 11, 1997. This simulation was used as the background for simulations of the May 12, 1997 CME. (b) May 13, 2005. This simulation is also the prelude to studies of the May 2005 CME. Much higher field strength in the active regions yields higher-than-observed emission with this heating model. (c) September 20, 2007. The Sun was very quiet during this time. An extended coronal hole is visible in the observations and the simulation. (d) July 19, 2008. This is the rotation prior to the August 8, 2008 eclipse. The Sun is again very quiet. The three left-most images are from EUVI aboard the STEREO A spacecraft. STEREO A views a different portion of the Sun than the Hinode spacecraft, where the XRT image on the right is taken from.*

wind plasma through the combined effects of wave damping and turbulent cascade (Cranmer et al., 2007; Cranmer, 2010). These approaches will have fewer free parameters and may eventually yield more accurate solutions than a purely empirical approach.

In Figure 2 we compare the observed images with those synthesized from our model for August 27, 1996, when the "Elephant's trunk" equatorial coronal hole was visible. To make a quantitative comparison, we processed SOHO/EIT observations using the SolarSoft package to produce images with absolute "DN/s" [data number/sec] values, in which the images are corrected for background dark current subtraction, degridding, filter normalization, response sensitivity correction, and exposure time normalization. We computed the emission from our MHD solutions by integrating the emission kernel, $\int n_e^2 f(T) ds$, over the line of sight with the appropriate emission and instrument response function $f(T)$. We plot the log of the emission with *identical* scales for the observed and simulated images. Although there are regions in which the emission is dissimilar, especially on small length scales and in the active region, the large scale features, especially the coronal hole regions, agree reasonably well.

Figure 3 shows comparisons of simulated and actual emission for four other time periods. Frame (a) shows results around the time of the May 12, 1997 CME, the same calculation illustrated in Figure 1. Figure 3 illustrates that a thermodynamic model, with empirically-based heating, is capable of reproducing the essential features of the observations for a number of time periods. Thus, in spite of the fact that the physical processes that heat the corona remain unknown, we have captured, at least to a first approximation, their effects within our model.

3 The WSA Model

Support from this program has allowed us to includes a version of the potential field source-surface/Wang-Sheeley-Arge (WSA) model in CORHEL to provide quick-look solutions. The well-known potential field source-surface model (PFSS) is a potential (current-free) approximation to the coronal magnetic field obtained by solving Laplace's equation ($\nabla^2 \Phi = 0$) assuming that the magnetic field becomes radial at a certain height (usually $2.5 R_0$, where R_0 is the solar radius). A variant of this model solves for the field above the source surface, under the assumption that regions of opposite magnetic polarity are separated by a current sheet (potential field current sheet or PFCS model). The WSA model empirically estimates the solar wind speed based on a combination of the expansion factor of the magnetic field and the distance of magnetic footpoints from coronal hole boundaries. Zoran Mikić at PSI and Nick Arge at AFRL have implemented the PFSS, PFCS, and WSA models using the modern numerical potential solver from the MAS code. Figure 4 shows an example of a WSA solution from our model.

Incorporating the WSA model in CORHEL provides a number of advantages. Solutions depend sensitively on the input magnetic maps. Very often, comparisons between models really turn out to be comparisons between how the input data was processed. CORHEL can provide WSA and MHD solutions using the same magnetic map and grid so that different approaches to coronal modeling can be directly compared using the same map. Second, as the magnetic maps are so important, the WSA solutions allow one to quickly examine the results for different observatories and different map filtering. Third, this new version of WSA allows the development of higher resolution potential field solutions than is possible with the

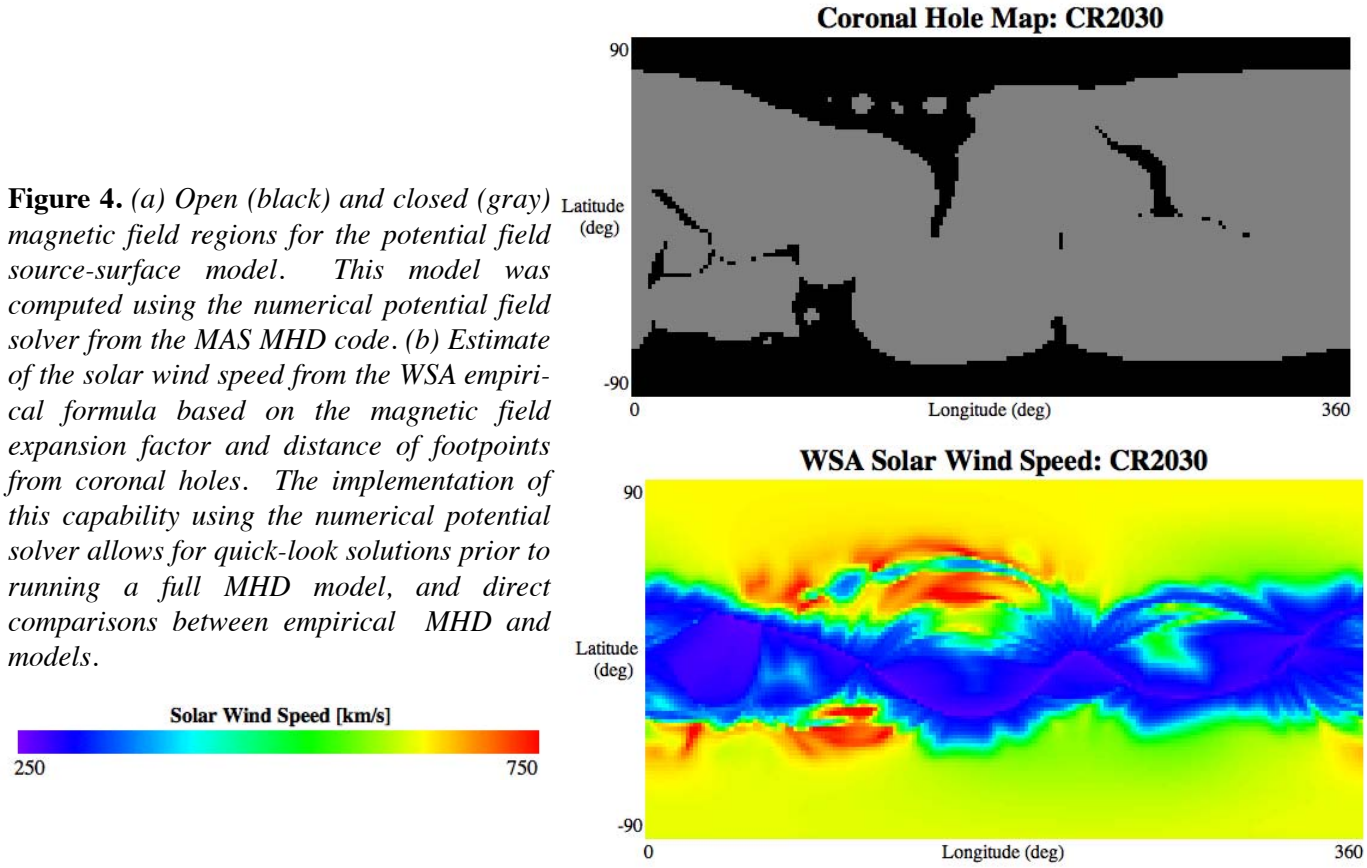

Figure 4. *(a) Open (black) and closed (gray) magnetic field regions for the potential field source-surface model. This model was computed using the numerical potential field solver from the MAS MHD code. (b) Estimate of the solar wind speed from the WSA empirical formula based on the magnetic field expansion factor and distance of footpoints from coronal holes. The implementation of this capability using the numerical potential solver allows for quick-look solutions prior to running a full MHD model, and direct comparisons between empirical MHD and models.*

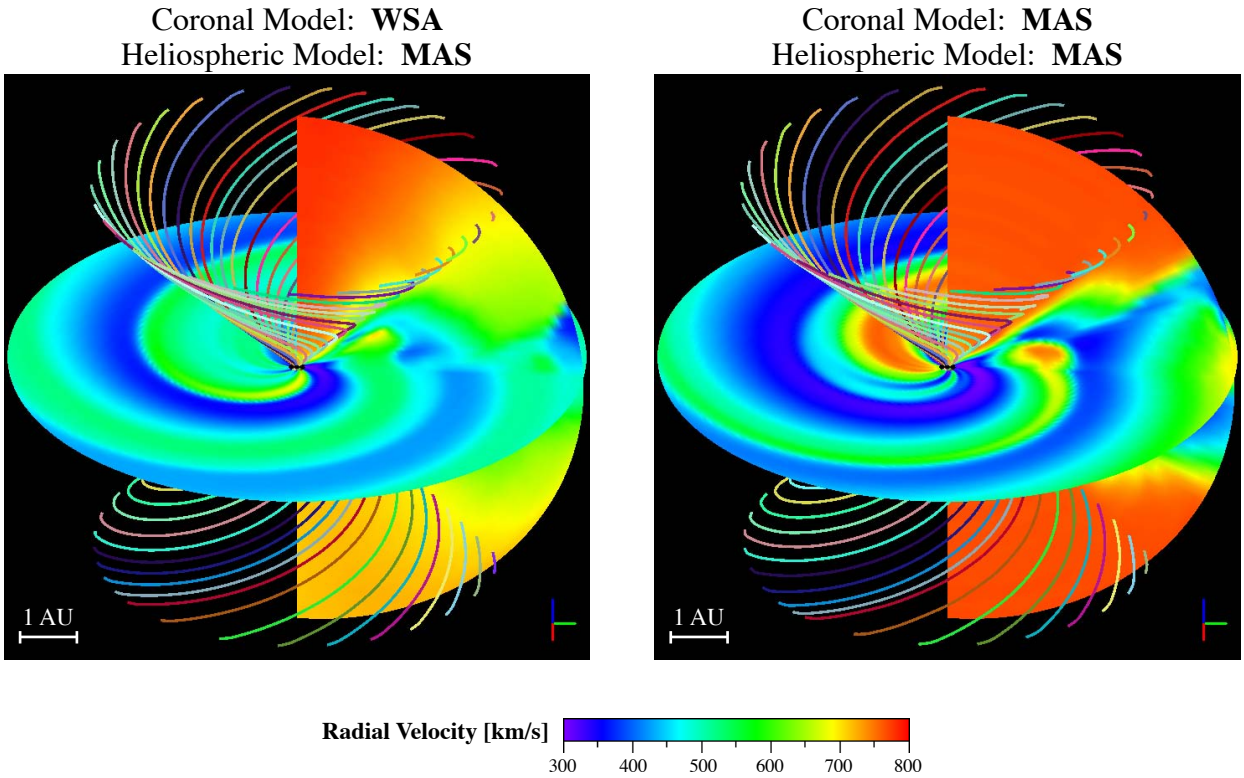

Figure 5. *Heliospheric solutions computed out to 5 AU for CR2068 (March 19-April 16, 2008, the WHI interval). Both solutions were computed with the MAS heliospheric model. Velocity color maps in a meridional slice and the equatorial plane are shown, together with selected magnetic field lines. The case on the left used the WSA model for the interior coronal solution and specification of the inner heliospheric boundary condition. The case on the right used the polytropic MAS coronal model. The stream interfaces are sharper and the high-speed streams are faster when the MHD model is used for the coronal solution.*

standard polynomial-based potential solvers, as well as nonuniform resolution (e.g. high resolution in a particular active region). This opens the possibility that further experimentation could improve these empirical solutions.

4 Heliospheric Models

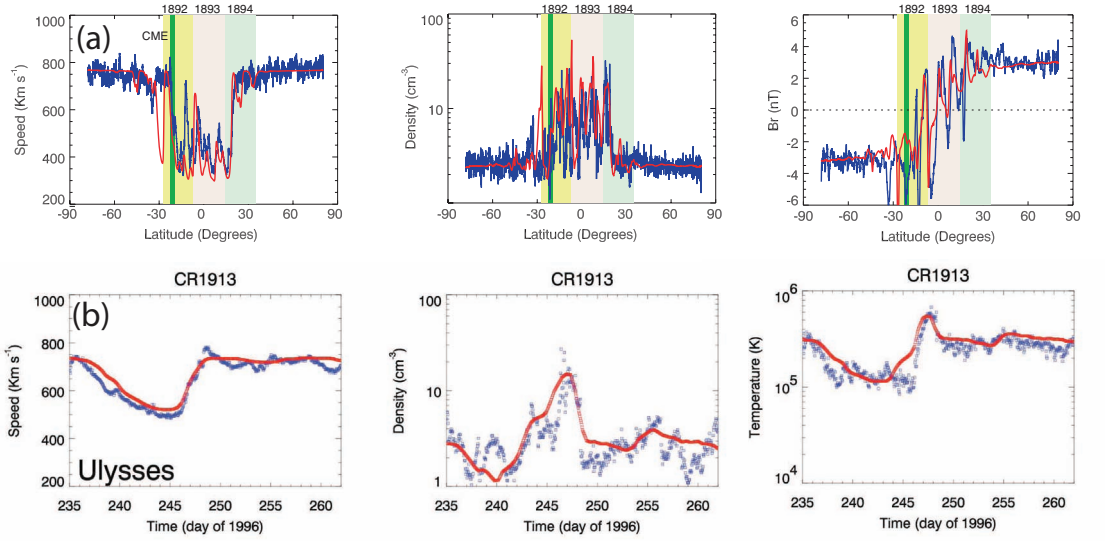

Figure 6: Comparison of model results (red) with observations (blue) for several time periods: (a) Ulysses rapid latitude scan; and (b) Carrington rotation 1913 (part of the "Whole Sun Month" interval), when Ulysses was located at $\sim 28°N$ heliographic latitude, at a distance of ~ 4.3 AU from the Sun, and on the opposite side of the Sun from Earth.

The three forms of coronal solutions described in sections 2 and 3 can be coupled to heliospheric models, with the results at the outer boundary of the coronal calculation supplying the inner boundary conditions for the heliospheric simulation. We briefly describe this coupling in Appendix A.2. We note here that both the WSA model and the polytropic MHD model require an ad hoc prescription for the boundary velocity to achieve realistic solutions. Even when a steady-state coronal solution is supplied to the heliospheric model, the heliospheric calculation is performed in the inertial frame and so becomes a time-dependent calculation. Two different heliospheric MHD models are now available in CORHEL; the Enlil model developed by Dusan Odstrcil, and a heliospheric version of the MAS model. Figure 5 shows an example of heliospheric solutions using both the WSA and the polytropic MAS model for the coronal solution. For both cases the heliospheric MAS model was used for the outer solution. Note that the high-speed streams are faster and the stream interfaces more sharply pronounced when the MAS model is used for the coronal solution. This appears to be a typical result regardless of which heliospheric code is used.

Our team at PSI have used global MHD models to interpret the observed properties of the quasi-steady corona and ambient solar wind (Riley et al., 1996, 2001a,b, 2002, 2003; Riley, 2007) for a number of years. In general, these models can reproduce the essential features of the observations. In Figure 6, for example, we compare model results (computed by "flying"

the spacecraft trajectories through the simulation results) with Ulysses observations during: (a) the so-called rapid latitude scan; and (b) CR 1913, at which time Ulysses was returning to lower latitudes and was located at $\sim 28°N$ at a distance of ~ 4.3 AU, and on the opposite side of the Sun from Earth. Comparisons like these demonstrate that the model can often reproduce the basic features of the solar wind under quiescent conditions. However, the model does not always perform so well, particularly when the coronal magnetic field evolves significantly from one rotation to the next. We believe that future models that use evolving boundary conditions could yield significantly more accurate solutions than have been possible in the past. The boundary conditions could be updated in time using a combination of new magnetograms as they become available and phototospheric flux evolution models (Arge et al., 2010).

For computing heliospheric solutions, we have developed two complementary approaches. In the simpler, ad hoc technique (illustrated above), we use the structure of the coronal magnetic field to derive the radial velocity boundary condition for the inner boundary of the heliospheric model. It is based on the idea that the slow solar wind originates at the boundary between open and closed field lines. We use the computed magnetic field from the coronal solution directly, and infer the remaining plasma quantities (density and temperature) by assuming momentum flux conservation and pressure balance over the sphere defining the inner boundary. The second, more self-consistent approach is to run the heliospheric model directly using all of the magnetic and plasma variables computed as part of the coronal solution. So far, the ad hoc solutions tend to better match in situ data at Earth and Ulysses, primarily because the transition from slow to fast wind is too gradual with our present heating/acceleration model. Eventually, we expect that as the physics contained within the coronal model becomes more sophisticated, and the remaining free parameters become better constrained, the quality of the self-consistently-derived heliospheric solutions will surpass the ad hoc results.

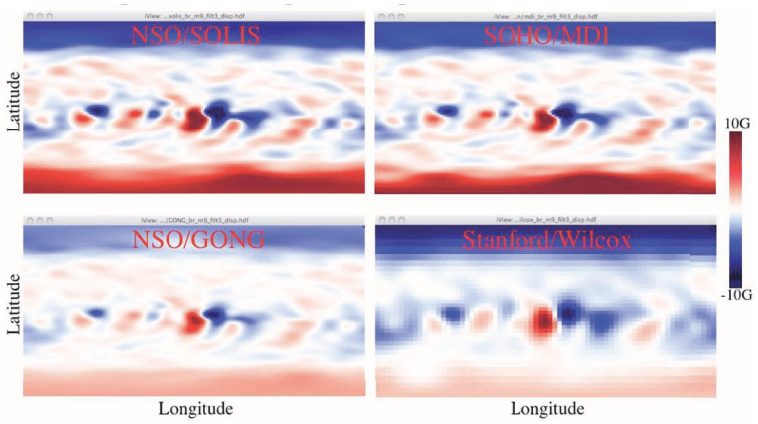

Figure 7: Comparison of synoptic maps (as a function of longitude and longitude, for four solar observatories. Synoptic Optical Long-term Investigations of the Sun (SOLIS), Michelson Doppler Imager (MDI); Global Oscillation Network Group (GONG); and Wilcox Solar Observatory (WSO). The Wang correction factor was applied to the WSO data.

5 Observationally-Derived Boundary Conditions

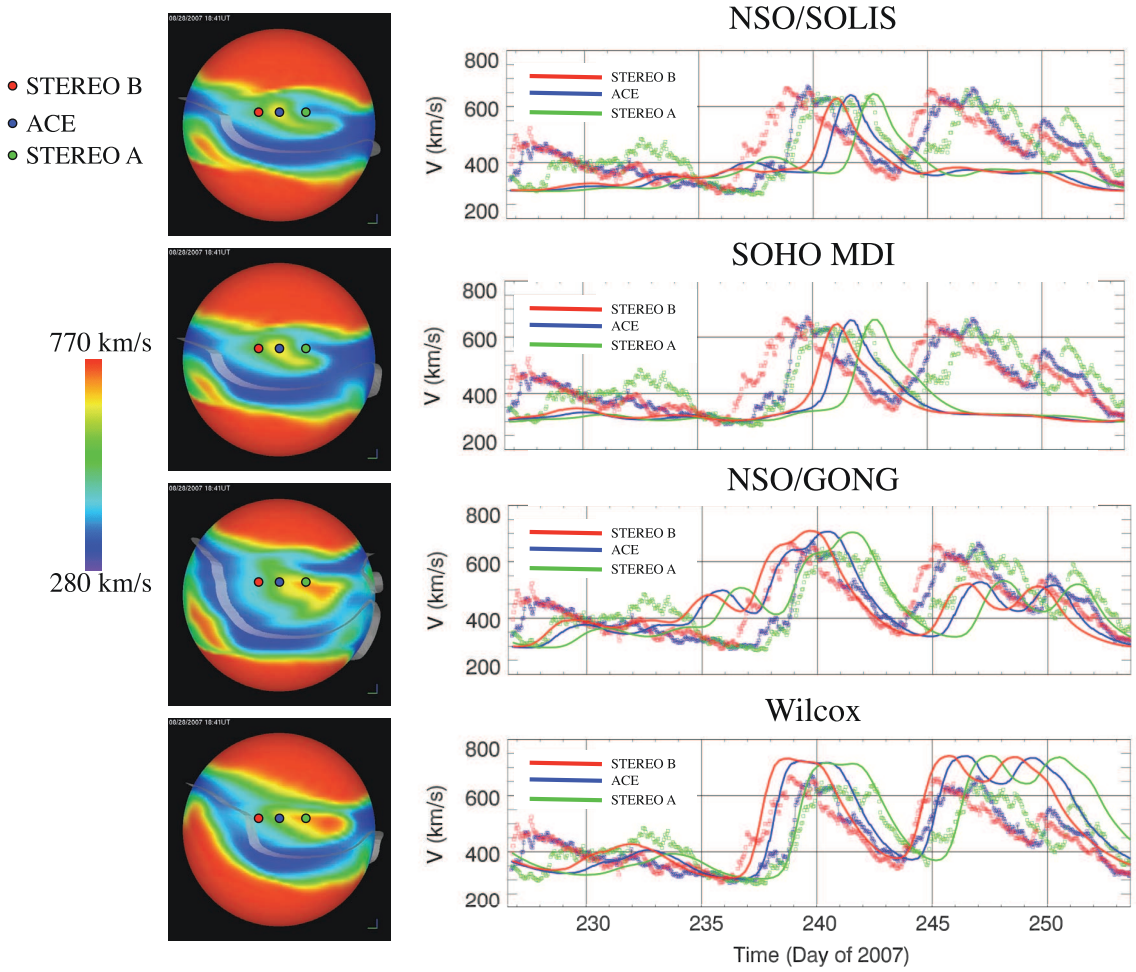

Figure 8: Predicted CORHEL solar wind velocity for Carrington Rotation 2060 (August 14 - September 10, 2007) using boundary conditions derived from (top to bottom): SOLIS, MDI aboard SOHO, NSO's GONG, and Wilcox Solar Observatory (maps shown in Fig. 7). The frames on the left show the velocity mapped on to a 1 AU sphere, viewed on day 241 (August 29, 2007) from Earth. The approximate locations of the STEREO A, B, and ACE spacecraft are shown. The position of the heliospheric current sheet for the different solutions is marked as a gray surface in these frames. The frames on the right show comparisons of the predicted flow speed with the STEREO A, B, and ACE spacecraft.

The Sun's magnetic field is a vital ingredient to any predictive model of the corona and solar wind. Full-disk measurements of the line-of-sight component of the magnetic field in the photosphere have been available for almost 40 years. As no consensus has emerged as to whether a specific observatory has the most accurate maps, we have designed CORHEL to allow the user to choose the the input data from a range of instruments. The user can select from 6 different magnetographs for the input boundary data: Mount Wilson Observatory (MWO); the National Solar Observatory Vacuum telescope at Kitt Peak (NSO/KP, for

dates prior to September, 2003); the NSO vector spectro-magnetograph (NSO/SOLIS, after September, 2003); NSO/GONG, the Michelson Doppler Imager aboard the SOHO spacecraft (MDI), and Wilcox Solar Observatory (WSO). Magnetograms are now available from the Helioseismic and and Magnetic Imager (HMI) aboard the SDO spacecraft launched in February, 2010, CORHEL will start using HMI magnetic maps when they become routinely available.

The magnetic maps supplied from different observatories usually agree very well qualitatively, but often differ quantitatively. These differences are not trivial and can lead to important differences in the solutions. As an illustration, Figure 7 summarizes synoptic maps as a function of longitude and latitude from four solar observatories for Carrington rotation 2060. The SOLIS, MDI, and GONG maps were interpolated to a lower resolution 180×90 resolution; the WSO is displayed at nonuniform 36×73 resolution (essentially the standard resolution that is available). The structures in the maps are similar, but there are quantitative differences in the magnitude of the fields. The global structure of the velocity predicted by the MHD models using these different maps is also qualitatively similar, as can be seen in the left hand frames of Figure 8. However, the velocity predicted for the STEREO and ACE spacecraft can differ significantly when different maps are used, as shown in the right hand frames of Figure 8. Because Earth sits in the slow wind band associated with the coronal streamer belt, the solar wind parameters are sensitive to quantitative differences in the maps, which can strongly influence the accuracy of the modeled solutions when compared with 1 AU measurements. Much of this difference may occur because of differing estimates for the polar fields. Our results indicate that the 1 AU results are also likely to be sensitive to changes in photospheric field that occur over the course of a solar rotation.

6 Summary

CORHEL is a coupled set of models and tools for quantitatively modeling the ambient solar corona and solar wind in various approximations. Support from the AFOSR/NASA/NSF partnership for Collaborative Space Weather Modeling has allowed us to greatly enhance the capabilities of CORHEL. CORHEL is available for community use at the CCMC, and is also being run by CISM and AFRL. We are presently working with the CCMC to enhance the user interface for selecting model parameters and diagnostic outputs. We have used CORHEL and/or its component models in a number of studies, as shown in the publications section.

A Appendix: Model Description

Figure 9 shows the present functionality of CORHEL. In sections A.1-A.3 we describe some details of CORHEL, including the equations, boundary and initial conditions for the coronal model, and coupling of coronal and heliospheric solutions.

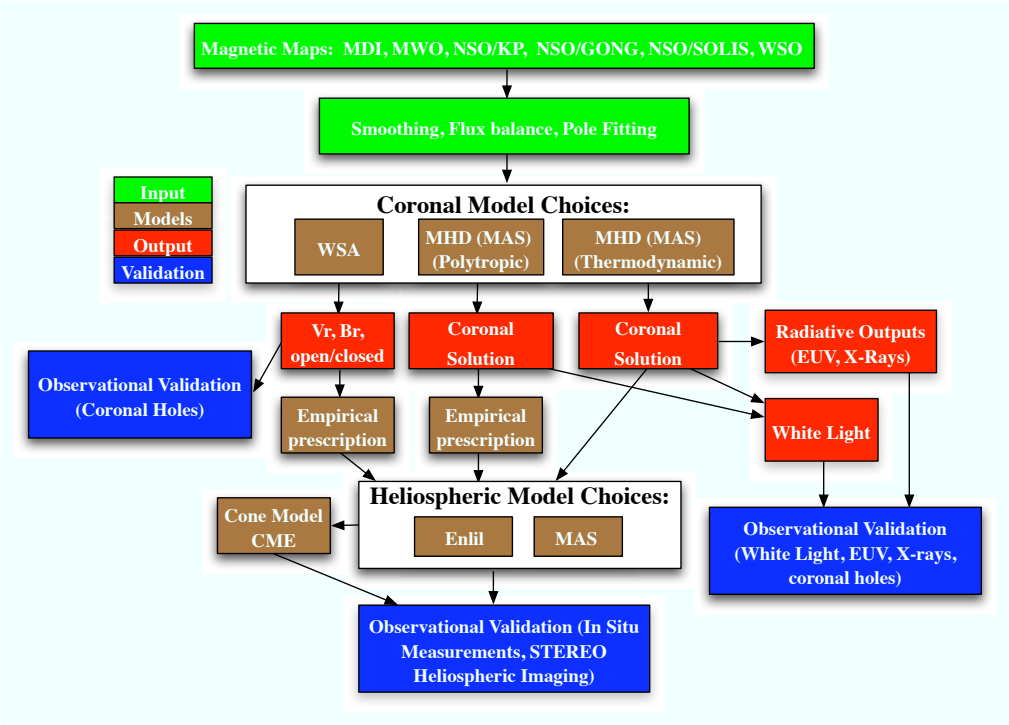

Figure 9: Flow chart depicting the present state of CORHEL. Green boxes indicate the primary input: data derived from measured solar magnetic fields. The coronal model encompasses three choices: WSA runs for immediate answers from a baseline model, polytropic MHD for quick turnaround runs, and thermodynamic MHD for the most physically realistic description. Red indicates coronal model output, including simulated emission and white light images. Coronal models feed into the heliospheric model (two choices) using either empirical prescriptions for the velocity, density, and temperature or directly driven by the outputs from the thermodynamic coronal model.

A.1 Coronal Modeling: Equations

The PSI coronal code MAS (Magnetohydrodynamic Algorithm outside a Sphere) solves the following equations in spherical coordinates:

$$\nabla \times \mathbf{B} = \frac{4\pi}{c}\mathbf{J}, \tag{1}$$

$$\nabla \times \mathbf{E} = -\frac{1}{c}\frac{\partial \mathbf{B}}{\partial t}, \tag{2}$$

$$\mathbf{E} + \frac{1}{c}\mathbf{v} \times \mathbf{B} = \eta \mathbf{J}, \tag{3}$$

$$\frac{\partial \rho}{\partial t} + \nabla \cdot (\rho \mathbf{v}) = 0, \tag{4}$$

$$\rho \left(\frac{\partial \mathbf{v}}{\partial t} + \mathbf{v} \cdot \nabla \mathbf{v} \right) = \frac{1}{c} \mathbf{J} \times \mathbf{B} - \nabla p - \nabla p_w + \rho \mathbf{g} + \nabla \cdot (\nu \rho \nabla \mathbf{v}), \tag{5}$$

$$\frac{1}{\gamma - 1} \left(\frac{\partial T}{\partial t} + \mathbf{v} \cdot \nabla T \right) = - T \nabla \cdot \mathbf{v} + S, \tag{6}$$

$$S = \frac{1}{2 k n_e} \left(- \nabla \cdot \mathbf{q} - n_e n_p Q(T) + H + H_d + D \right) \tag{7}$$

where $\mathbf{B}$ is the magnetic field, $\mathbf{J}$ is the current density, $\mathbf{E}$ is the electric field, ρ, $\mathbf{v}$, p, and T are the plasma mass density, velocity, pressure, and temperature, respectively, n_e is the electron density, and p_w is the wave pressure and represents the acceleration due to waves. The gravitational acceleration is $\mathbf{g} = -g_0 \hat{\mathbf{r}} R_0^2 / r^2$, R_0 is the solar radius, $\gamma = 5/3$ is the ratio of specific heats, η is the resistivity, and ν is the viscosity. The plasma pressure is $p = (n_e + n_p) k T$, where for a hydrogen plasma, $n_e = n_p$, and $\rho = m_p n_p$, where m_p is the proton mass. In practice, the vector potential $\mathbf{A}$ is used to advance the equations. These equations are solved on nonuniform meshes that allow us to concentrate grid points in regions of interest. The method of solution, including the boundary conditions, has been described previously (Mikić & Linker, 1994; Linker & Mikić, 1997; Lionello et al., 1999; Mikić et al., 1999; Linker et al., 2001; Lionello et al., 2001). The equations are solved on staggered meshes, which facilitates the implementation of boundary conditions and enforces the vector identifies $\nabla \cdot \nabla \times = \nabla \times \nabla = 0$ to round-off error. This approach ensures that $\nabla \cdot \mathbf{B} = 0$ in the calculation.

In the energy equation (6)–(7), H is the coronal heating source, $H_d = \eta J^2 + \nu \nabla \mathbf{v} : \nabla \mathbf{v}$ is the heating due to resistive and viscous dissipation, D is the heating due to dissipation of Alfvén waves, n_e and n_p are the electron and proton density, and $Q(T)$ is the radiation loss function (e.g., Rosner et al., 1978; Athay, 1986). In the collisional regime (below $\sim 10 R_0$), the heat flux is given by $\mathbf{q} = -\kappa_\parallel \hat{\mathbf{b}} \hat{\mathbf{b}} \cdot \nabla T$, where $\hat{\mathbf{b}}$ is the unit vector along $\mathbf{B}$, and $\kappa_\parallel = 9 \times 10^{-7} T^{5/2}$ is the Spitzer value of the parallel thermal conductivity (in cgs units). In the collisionless regime (beyond $\sim 10 R_0$), the heat flux is given by $\mathbf{q} = \alpha n_e k T \mathbf{v}$, where α is a dimensionless parameter of order 1 (Hollweg, 1978). The (unknown) coronal heating source H is a parameterized function, as discussed in section 2.1.

Since the acceleration of the solar wind by Alfvén waves occurs on spatial and time scales below those of our global numerical model, the wave pressure p_w is evolved using an equation for the time-space averaged Alfvén wave energy density ε. In the present version of the model, we use the WKB approach (Jacques, 1977; Usmanov et al., 2000):

$$\frac{\partial \varepsilon}{\partial t} + \nabla \cdot \mathbf{F} = \mathbf{v} \cdot \nabla p_w - D, \tag{8}$$

where $\mathbf{F} = (\frac{3}{2} \mathbf{v} + \mathbf{v_A}) \varepsilon$ is the Alfvén wave energy flux, $v_A = B / \sqrt{4 \pi \rho}$ is the Alfvén speed, and $p_w = \frac{1}{2} \varepsilon$. The Alfvén wave velocity is $\mathbf{v_A} = \pm \hat{\mathbf{b}} v_A$; we transport two Alfvén wave fields (waves parallel and antiparallel to $\mathbf{B}$), which are combined to give ε. The Alfvén wave energy density ε is related to the space-time average of the fluctuating component of the magnetic field δB by $\varepsilon = \langle \delta B^2 \rangle / 4 \pi$. The dissipation term D expresses the nonlinear dissipation of Alfvén waves in interplanetary space and is modeled phenomenologically (Hollweg, 1978). We are presently

experimenting with a more fundamental wave-driven turbulence model (Cranmer et al., 2007; Cranmer, 2010).

The simplified polytropic model is obtained by setting $p_w = 0$ in Eq. (5), $S = 0$ in Eq. (7), and γ close to 1 (e.g., $\gamma = 1.05$). The polytropic model is popular because it reduces the numerical requirements for 3D coronal calculations.

The MHD equations in the corona are very stiff, since they span multiple time and length scales. In a typical coronal calculation, one can have mesh cells as small as $\sim 100\,\mathrm{km}$, and as large as a few solar radii ($\sim 10^6\,\mathrm{km}$). The Alfvén and sound speeds can range from $\sim$20 km/s to $\sim$10,000 km/s. The Lundquist number can be $\sim 10^5$. For these equations, implicit methods are crucial. Typically, we exceed the wave Courant number (which would limit the time step in an explicit calculation) by factors of 50–100, and we greatly exceed the time steps needed for stable advancement of diffusive terms (thermal conductivity, resistivity, and viscosity). We use a semi-implicit technique to provide unconditional stability to Alfvén and sound waves (Mikić et al., 1988; Harned & Kerner, 1985; Harned & Schnack, 1986; Schnack et al., 1987), and fully implicit advancement of diffusive terms. The very large sparse matrices arising from these methods are inverted using an iterative preconditioned Conjugate Gradient method.

The MAS code is written in FORTRAN95 using the Message Passing Interface (MPI) with three-dimensional domain decomposition. The code is portable and runs on many systems (including Mac OS X and various flavors of Linux that are used on NASA's and NSF's massively parallel computer architectures). We are able to perform runs with tens of millions of mesh points on hundreds to thousands of processors.

A.2 Coronal Modeling: Initial Conditions, Boundary Conditions, and Solution Procedure

The initial and boundary conditions for our models of the solar corona are described in detail by Linker & Mikić (1997). The key boundary condition required from observations is the radial magnetic field at the solar surface, B_{r0}. This must be supplemented with conditions on the plasma temperature and density at $r = R_0$. In polytropic models, these are coronal values typically in the range of $T_0 = 1.4 - 2 \times 10^6\,\mathrm{K}$ and $n_0 = 1 - 4 \times 10^8\,\mathrm{cm}^{-3}$. The choice of values influences the relative size of the closed and open field regions and the speed of the solar wind. In thermodynamic models, $T_0 = 20{,}000\,\mathrm{K}$ and $n_0 = 2 \times 10^{12}\,\mathrm{cm}^{-3}$, representative of the upper chromosphere. In these models, the choices for coronal heating determine the properties of the solutions, and the exact choice of T_0 and n_0 are not crucial as long as n_0 is large enough to maintain a chromosphere in the presence of the specified heating. For both polytropic and thermodynamic models, the velocity parallel to the magnetic field cannot be specified in a well-posed problem; it is determined self-consistently at $r = R_0$ from the characteristic equations along $\mathbf{B}$. At the upper boundary, where the flow is supersonic and super-Alfvénic, all quantities are computed from characteristic equations.

For the initial condition, we start by computing a potential magnetic field in the corona that matches B_{r0} at the solar surface. We impose a spherically symmetric solar wind solution and integrate the time-dependent MHD equations in time until the solution settles down to an equilibrium. Helmet streamers with closed field lines form, surrounded by open field lines along which the solar wind flows outward.

A.3 Heliospheric Solutions

To compute heliospheric solutions, the results at the outer boundary of the coronal calculation must supply the inner boundary conditions for the heliospheric simulation. The interface between the coronal and heliospheric regions is located in the super-critical flow region, usually between $20R_0$ and $30R_0$. This makes the coupling procedure relatively straightforward, since information is passed only one way: from the coronal model to the heliospheric model. Because the physics of the coupling is not complicated, a sophisticated coupling architecture is not required. The coupling is accomplished by reading and writing files in a specified format. The procedure is very modular because any coronal or heliospheric model can be substituted; the models just have to be capable of reading/writing files in the designated format.

To produce realistic solar wind solutions in the inner heliosphere, the WSA model uses an empirical prescription to set the plasma properties at the inner boundary of the heliospheric model. Polytropic coronal models lack the necessary physics to predict realistic contrast between the fast and slow wind. Therefore, we also use an empirical technique (Riley et al., 2001a) to specify the inner boundary conditions for the velocity; this specification has some similarities to the WSA specification. An advantage of the thermodynamic MHD model (section 2.1) is that such a specification is not necessary. Given a specified model for the coronal heating and solar wind acceleration, fast and slow wind regions are produced self-consistently in the coronal model and can be fed directly to the heliospheric model. Even in the case of a steady-state coronal solution, the heliospheric solutions are time-dependent. This is because the steady-state coronal input co-rotates in the inertial frame of the heliospheric calculation.

Both the MAS and Enlil heliospheric models in CORHEL solve ideal or nearly ideal versions of Eqs. (1-6). The outer boundary conditions are again in the regime of supersonic and super-Alfvénic flow and are computed using characteristic equations.

Publications Supported by AFOSR-NASA-NSF Strategic Capabilities Program

Abramenko, V., Yurchyshyn, V., Linker, J., Mikić, Z., Luhmann, J., and Lee, C. O. (2010). Low-Latitude Coronal Holes at the Minimum of the 23rd Solar Cycle. ApJ, 712:813–818.

Antiochos, S. K., Mikić, Z., Titov, V. S., Lionello, R., and Linker, J. A. (2011). A model for the sources of the slow solar wind. ApJ*, to appear*, 730.

Aschwanden, M. J., Burlaga, L. F., Kaiser, M. L., Ng, C. K., Reames, D. V., Reiner, M. J., Gombosi, T. I., Lugaz, N., Manchester, W., Roussev, I. I., Zurbuchen, T. H., Farrugia, C. J., Galvin, A. B., Lee, M. A., Linker, J. A., Mikić, Z., Riley, P., Alexander, D., Sandman, A. W., Cook, J. W., Howard, R. A., Odstrčil, D., Pizzo, V. J., Kóta, J., Liewer, P. C., Luhmann, J. G., Inhester, B., Schwenn, R. W., Solanki, S. K., Vasyliunas, V. M., Wiegelmann, T., Blush, L., Bochsler, P., Cairns, I. H., Robinson, P. A., Bothmer, V., Kecskemety, K., Llebaria, A., Maksimovic, M., Scholer, M., and Wimmer-Schweingruber, R. F. (2008). Theoretical modeling for the stereo mission. *Space Science Reviews*, 136:565–604.

Case, A. W., Spence, H. E., Owens, M. J., Riley, P., and Odstrcil, D. (2008). Ambient solar wind's effect on ICME transit times. Geophys. Res. Lett., 35:15105–+.

Ko, Y.-K., Li, J., Riley, P., and Raymond, J. C. (2008). Large-Scale Coronal Density and Abundance Structures and Their Association with Magnetic Field Structure. ApJ, 683:1168–1179.

Lee, C. O., Luhmann, J. G., Odstrcil, D., MacNeice, P. J., de Pater, I., Riley, P., and Arge, C. N. (2009). The Solar Wind at 1 AU During the Declining Phase of Solar Cycle 23: Comparison of 3D Numerical Model Results with Observations. Sol. Phys., 254:155–183.

Lepri, S. T., Antiochos, S. K., Riley, P., Zhao, L., and Zurbuchen, T. H. (2008). Comparison of Heliospheric In Situ Data with the Quasi-steady Solar Wind Models. ApJ, 674:1158–1166.

Linker, J. A., Lionello, R.and Mikić, Z., Titov, V. S., and Antiochos, S. K. (2011). The evolution of open magnetic flux: MHD simulations. ApJ*, to appear*, 730.

Lionello, R., Linker, J. A., and Mikić, Z. (2009). Multispectral Emission of the Sun During the First Whole Sun Month: Magnetohydrodynamic Simulations. ApJ, 690:902–912.

Luhmann, J. G., Li, Y., Riley, P., Arge, C. N., Liu, Y., and Detoma, G. (2008). Challenges Created by Active Regions in Global Models for Space Weather Uses. In Howe, R., Komm, R. W., Balasubramaniam, K. S., and Petrie, G. J. D., editors, *Subsurface and Atmospheric Influences on Solar Activity*, volume 383 of *Astronomical Society of the Pacific Conference Series*, pages 133–+.

Odstrcil, D., Pizzo, V. J., Arge, C. N., Bissi, M. M., Hick, P. P., Jackson, B. V., Ledvina, S. A., Luhmann, J. G., Linker, J. A., Mikic, Z., and Riley, P. (2008). Numerical Simulations

of Solar Wind Disturbances by Coupled Models. In Pogorelov, N. V., Audit, E., and Zank, G. P., editors, *Numerical Modeling of Space Plasma Flows*, volume 385 of *Astronomical Society of the Pacific Conference Series*, pages 167–+.

Riley, P. (2007a). An Alternative Interpretation of the Relationship between the Inferred Open Solar Flux and the Interplanetary Magnetic Field. ApJ, 667:L97–L100.

Riley, P. (2007b). Modeling corotating interaction regions: From the Sun to 1 AU. *Journal of Atmospheric and Terrestrial Physics*, 69:32–42.

Riley, P. (2010). The Three-Dimensional Structure of the Inner Heliosphere. *Twelfth International Solar Wind Conference*, 1216:323–328.

Riley, P. and Gosling, J. T. (2007). On the origin of near-radial magnetic fields in the heliosphere: Numerical simulations. *Journal of Geophysical Research (Space Physics)*, 112:6115–+.

Riley, P., Linker, J. A., Lionello, R., Z., M., and Luhmann, J. (2010a). Global MHD Modeling of the Solar Corona and Inner Heliosphere for the Whole Heliosphere Interval. *Accepted for publication in Sol. Phys.*

Riley, P., Linker, J. A., Mikic, Z., and Lionello, R. (2008). Global MHD Modeling of the Solar Wind and CMEs: Energetic Particle Applications. In *American Institute of Physics Conference Series*, volume 1039 of *American Institute of Physics Conference Series*, pages 279–285.

Riley, P., Luhmann, J., Opitz, A., Linker, J. A., and Mikic, Z. (2010b). Interpretation of the cross-correlation function of ACE and STEREO solar wind velocities using a global MHD Model. *J. Geophys. Res. (Space Physics)*, 115:11104–+.

Riley, P., Mikic, Z., Lionello, R., Linker, J. A., Schwadron, N. A., and McComas, D. J. (2010c). On the relationship between coronal heating, magnetic flux, and the density of the solar wind. *J. Geophys. Res.*, 115:6104–+.

Rušin, V., Druckmüller, M., Aniol, P., Minarovjech, M., Saniga, M., Mikić, Z., Linker, J. A., Lionello, R., Riley, P., and Titov, V. S. (2010). Comparing eclipse observations of the 2008 August 1 solar corona with an MHD model prediction. A&A, 513:A45+.

Titov, V. S., Forbes, T. G., Priest, E. R., Mikić, Z., and Linker, J. A. (2009). Slip-Squashing Factors as a Measure of Three-Dimensional Magnetic Reconnection. ApJ, 693:1029–1044.

Titov, V. S., Mikic, Z., Linker, J. A., and Lionello, R. (2008). 1997 May 12 Coronal Mass Ejection Event. I. A Simplified Model of the Preeruptive Magnetic Structure. ApJ, 675:1614–1628.

Titov, V. S., Mikić, Z., Linker, J. A., Lionello, R., and Antiochos, S. K. (2011). Magnetic Topology of Coronal Hole Linkages. ApJ*, to appear*, 730.

References

Arge, C. N., Henney, C. J., Koller, J., Compeau, C. R., Young, S., MacKenzie, D., Fay, A., & Harvey, J. W. 2010, Twelfth International Solar Wind Conference, 1216, 343

Athay, R. G. 1986, Ap. J., 308, 975

Buchlin, E., & Velli, M. 2007, Ap. J., 662, 701

Cohen, O., Sokolov, I. V., Roussev, I. I., & Gombosi, T. I. 2008, Journal of Geophysical Research (Space Physics), 113, 3104

Cranmer, S. R. 2010, Ap. J. Lett., 710, 676

Cranmer, S. R., van Ballegooijen, A. A., & Edgar, R. J. 2007, ApJS, 171, 520

Harned, D. S., & Kerner, W. 1985, J. Comp. Phys., 60, 62

Harned, D. S., & Schnack, D. D. 1986, J. Comp. Phys., 65, 57

Hayashi, K., Zhao, X. P., & Liu, Y. 2008, Journal of Geophysical Research (Space Physics), 113, 7104

Hollweg, J. V. 1978, Rev. of Geophys. and Space Phys., 16, 689

Hollweg, J. V. 2003, in AIP Conf. Proc. 679: Solar Wind Ten, 14–20

Jacques, S. A. 1977, Ap. J., 215, 942

Linker, J. A., Lionello, R., Mikić, Z., & Amari, T. 2001, J. Geophys. Res., 106, 25165

Linker, J. A., Lionello, R., Mikić, Z., Riley, P., & Titov, V. 2007, in American Astronomical Society Meeting Abstracts, Vol. 210, American Astronomical Society Meeting Abstracts, #58.05–+

Linker, J. A., & Mikić, Z. 1997, Coronal Mass Ejections, 99, 269, edited by N. Crooker, J. Joselyn, and J. Feynmann, p. 269, AGU, Washington, D. C.

Lionello, R., Linker, J. A., & Mikić, Z. 2001, Ap. J., 546, 542

Lionello, R., Linker, J. A., & Mikić, Z. 2009, Ap. J., 690, 902

Lionello, R., Mikić, Z., & Linker, J. A. 1999, J. Comp. Phys., 152, 346

Mikić, Z., Barnes, D. C., & Schnack, D. D. 1988, Ap. J., 328, 830

Mikić, Z., & Linker, J. A. 1994, Ap. J., 430, 898

Mikić, Z., & Linker, J. A. 1996, in International Solar Wind 8, ed. e. a. Winterhalter, D., Vol. 382, AIP Conf. Proceedings, 104

Mikić, Z., Linker, J. A., Schnack, D. D., Lionello, R., & Tarditi, A. 1999, Phys. Plasmas, 6, 2217

Odstrcil, D., Pizzo, V. J., & Arge, C. N. 2005, J. Geophys. Res., 110, 2106

Odstrcil, D., Pizzo, V. J., Riley, P., & Arge, C. N. 2004, AGU Fall Meeting Abstracts, A1+

Osterbrock, D. E. 1961, Ap. J., 134, 347

Parker, E. N. 1972, Ap. J., 174, 499

—. 1994, Spontaneous current sheets in magnetic fields: with applications to stellar x-rays (New York, Oxford University Press)

Piddington, J. H. 1956, MNRAS, 116, 314

Rappazzo, A. F., Velli, M., Einaudi, G., & Dahlburg, R. B. 2007, Ap. J. Lett., 657, L47

Riley, P. 2007, JASTP, 69, 32

Riley, P., Gosling, J. T., Weiss, L. A., & Pizzo, V. J. 1996, J. Geophys. Res., 101, 24349

Riley, P., Linker, J. A., & Mikić, Z. 2001a, J. Geophys. Res., 106, 15889

—. 2002, J. Geophys. Res., 107, DOI 10.1029/2001JA000299

Riley, P., Linker, J. A., Mikić, Z., & Lionello, R. 2001b, in Space Weather, Geophysical Monograph Series, ed. P. Song, H. J. Singer, & G. L. Siscoe, Vol. 125 (Washington, DC: AGU), 159

Riley, P., Mikić, Z., & Linker, J. A. 2003, Ann. Geophys., 21, 1347

Roberts, B. 2000, Sol. Phys., 193, 139

Rosner, R., Tucker, W. H., & Vaiana, G. S. 1978, Ap. J., 220, 643

Schnack, D. D., Barnes, D. C., Mikić, Z., Harned, D. S., & Caramana, E. J. 1987, J. Comp. Phys., 70, 330

Usmanov, A. V., Goldstein, M. L., Besser, B. P., & Fritzer, J. M. 2000, J. Geophys. Res., 105, 12675

Velli, M. 2003, Plasma Physics and Controlled Fusion, 45, A205

Webb, D. F., Lepping, R. P., Burlaga, L. F., DeForest, C. E., Larson, D. E., Martin, S. F., Plunkett, S. P., & Rust, D. M. 2000, J. Geophys. Res., 105, 27251